Electronic Supplementary Material (ESI) for Lab on a Chip.

Supplementary Information

Multifunctional Droplet Handling on Surface-charge-graphic-decorated Porous Papers

*Jiayao Wu, Duokui Fang, Yifan Zhou, Ge Gao, Ji Zeng, Yubin Zeng, and Huai Zheng**

This PDF file includes:

Supplementary Text:

Other Supplementary Materials for this manuscript include the following:

Movies S1 to S10

Supplementary Text:

1. The droplet actuation platform

1.1 The structure of the platform

The platform is a simple structure, as shown in **Figure S1**, consisting of a pair of needle electrodes, a battery-driven voltage source, oil-impregnated porous papers, a syringe pump (Ditron Technology, LSP01-1B, China), and a three-axis digital moving platform. The bottom needle electrode is grounded and installed on the gripper of the three-axis digital moving platform. The battery-driven voltage source is compact (130 mm*65 mm*57 mm), and consists of rechargeable lithium-ion batteries (Chenke, 12V-18650, China), a high-voltage power module (Corso Electronic, KDHM-Q-12S15000P-VI, China), and a metal enclosure, as shown in **Figure S2**.

As the key device of the droplet actuation platform, the three-axis digital moving platform can be divided into two parts: hardware and software. The hardware consists of micro motors (Ruite, 42-CM04, China), screw guides (Lizhou, FK-1605, China), and Arduino, which is built by our team. And the software used is Kvenjoy,[1] which is widely used in laser processing/writing robots. The motion resolution of the current platform is up to 0.25 mm, and higher motion resolution can be achieved by improving the hardware. Moreover, the three-axis platform provides two methods of control. One is to pre-program multiple routes/modes in the software, with no time delay in new routes/modes switching, which is suitable for automated operation. The other is to operate the controller directly for real-time manipulation, which is suitable for personalized operation.

1.2 The universality of the platform

To verify the universality of this platform, we test various porous insulating papers and droplet materials. Porous insulating papers include PP papers, PTFE papers, PVDF papers, kraft papers, and baking oiled papers. Droplet materials include DI water, $FeCl_3$ solution, HCl solution, NaOH solution, pH indicator, alcohol, and food dye. **Figure S3** shows that the time-lapse trajectories of the $FeCl_3$ solution on the PP papers, DI water

on the PVDF papers, alcohol on the PTFE papers, and the dyes on the kraft papers and baking papers are actuated, respectively. It is observed that all droplets on oil-impregnated porous insulating papers show effective actuation. **Figure S4** displays the droplet dynamics on a dense PET film without a porous structure. The droplet is not actuated under the same electrical stimuli.

In principle, all conductive fluids and insulating films with porous structures can be applied in the presented droplet handling. The reason that we chose paper as the substrate is not only its high electrical insulation properties and chemical resistance but also its low cost and versatility,[2] which is very suitable in some cases where substrates need to be replaced at each experiment.

2. Revealing the mechanism of the droplet actuation

2.1 Electrical measurement

2.1.1 Current measurement

To initially verify the mechanism of the droplet actuation, the current of corona discharge and the surface current of porous insulating paper are measured by a high-precision high-speed electrometer (Keithley, 6517B, USA), as shown in **Figure S6**. **Figure S7** shows the measured current of corona discharge, which increases with the applied voltage. We find that the corona discharge starts at an applied voltage of 5 kV. The current is only ~2.3 μA at applied voltages up to 14 kV, and the power consumption is super low (~32 mW).

The measurement of the surface current of porous insulating paper is shown in Figure S6ii. A copper sheet (diameter 1 mm, thickness 130 μm) connected to the electrometer is placed at the tested point to receive the charges from corona discharge. The top and bottom needle electrodes are applied at 9 kV and -5 kV, respectively. As shown in **Figure S8**, the current is negative at the center (above the bottom electrode) and gradually increases to become positive as the radial distance expands. It suggests that the upward drifting negative charges from the bottom needle electrode during corona discharge penetrate the porous paper and deposit on the upper surface. The deposition

range of negative charges (D) is related to the distance of the bottom needle electrode from the porous paper (H_2). Comparing the current distribution for H_2 = 5 mm and H_2 = 10 mm shows that increasing the value of H_2 expands the deposition range of negative charges, which coincides with the Warburg formula. [3]

We also measure the surface current of the porous insulating paper with the hole arrays mask attached. As shown in **Figure S9**, at the originally-negatively-charged locations, the currents turn from negative to positive, while the current direction of the area above the holes has no change. It proves that the mask can act as a barrier (preventing charge penetration into the porous paper) for charge graphics.

All measured current results of porous paper surfaces indicate that there are negative charge areas above the bottom needle electrode and positive charges in the other area. Masks can effectively modulate charge distributions.

2.1.2 Potential measurement

The surface potential can be measured offline by an electrostatic voltmeter (341B, Trek, USA). [4] With a movable probe that is installed on the X-Y stage (**Figure S10**a), the electrostatic voltmeter can directly scan the surface and obtain the 2D surface potential distributions of porous paper. However, the surface potential of porous insulating paper cannot be obtained offline based on the electrostatic voltmeter, because the porous structure can diffuse charge leading to disordered charge graphics in the offline case. Therefore, we measure the surface potential of the mask (PET film) with/without holes offline to directly reveal the charge transferable through the hole structure. The surface potential of the mask without holes is uniformly positive (~100 V) (Figure S10b), while the surface potential of the mask with holes is negative around the holes and remains positive in another area (Figure S10c). Both surface potential and surface current measurement results confirm that negative charges can penetrate porous paper and deposit on its upper surface.

2.2 Electrostatic simulations

2.2.1 Simulation models

The needle-needle electrode doped with different dielectric layers is modeled by using the COMSOL electrostatic module and the PDE partial differential equation module, [5] as shown in **Figure S11**. The electric field strength at the surface of the electrode tips and the spatial charge density of the corona discharge obey the control equations as follows. [6,7]

$$\boldsymbol{E} = -\nabla \cdot V \tag{1}$$

$$\nabla \cdot \boldsymbol{D} = \rho_v \tag{2}$$

$$\boldsymbol{D} = \varepsilon_0 \varepsilon_r \boldsymbol{E} \tag{3}$$

$$\nabla \cdot (\pm \mu \boldsymbol{E} \rho_{\pm} \mp \boldsymbol{D}_{\pm} \nabla \cdot \rho_{\pm}) = -R_i \rho_+ \rho_- / q_e \tag{4}$$

where $\boldsymbol{E}$ is the electric field strength, V is the electric potential, $\boldsymbol{D}$ is the electric displacement, ρ_v is the spatial charge density, ρ_+, ρ_- are the spatial charge density of positive and negative charges, ε_0 is the permittivity of the air, $\varepsilon_0 = 1.00053$, used from the default materials of the COMSOL library, ε_r is the relative permittivity, $\varepsilon_r = 2.3$,[8] μ is the mobility of positive and negative charge, $\boldsymbol{D}_+$, $\boldsymbol{D}_-$ are the diffusion coefficients of positive and negative charges. R_i is the rate constant for ion-ion recombination, and q_e is the charge of electrons.

The boundary conditions for the spatial charge density at the electrode tips are derived iteratively from the Kaptsov assumption, and the electric field strength at the surface of the electrode tip is given by Peek's empirical law for air. [9,10]

$$E = 31(kV/cm) \cdot [1 + 0.308/(0.5R)^{1/2}] \tag{5}$$

$$\rho_{\pm} = I/(\mu E a) \tag{6}$$

where R is the radius of electrode tips in cm, a is the area of electrode tips, and I is the corona discharge current given in **Figure S7**.

According to Gauss's law, the boundary conditions for the charge density at a material interface equals the jump in the normal component of the displacement field.

$$\boldsymbol{n} \cdot (\boldsymbol{D_2} - \boldsymbol{D_1}) = \rho_s \tag{7}$$

where $\boldsymbol{n}$ is the normal vector at the material interface. $\boldsymbol{D_1}$ and $\boldsymbol{D_2}$ are the electric displacement vectors into and through the material interface respectively. ρ_s is the surface charge at the material interface.

We also inverse the surface charge density of the PET film based on COMSOL

software, as shown in **Figure S12**. The boundary conditions for surface potential are set according to the experimental results measured by the electrostatic voltmeter (341B, Trek, USA). The bottom surface of the PET film is electrically grounded. Other boundaries are set as Neumann boundary conditions. The surface charge density σ can be calculated by the following **Equation S8**.

$$\sigma = cU = \varepsilon\varepsilon_0 U/d \tag{8}$$

where U is the surface potential given by Fig. S10, c is the capacitance per area of the PET layer, $\varepsilon\varepsilon_0$ is the permittivity, and d is the thickness of the PET layer, respectively.

2.2.2 Simulation results

The simulation results of the surface charge density distribution of the porous insulating paper are shown in Figure 1fi. The simulation results show that the negative charges (up to -0.85 μC/m^2) are deposited at the center of the porous paper (above the bottom needle electrode), while positive charges are deposited at the rest of the area, forming a charge-graphic. The simulation results of the surface potential distribution corresponding to the charge-graphic are shown in Figure 1fii. The potential is low at the center of the porous paper surface (above the bottom needle electrode), while the potential gradually increases at the rest of the area, forming an EPW.

The simulation results of the surface charge density distributions of the PET film are shown in **Figure S13**. The simulation results show that the PET film surface without holes deposits positive charges uniformly (~12 μC/m^2). The PET film surface with holes forms a charge graphic, with negative charges (up to -4 μC/m^2) deposited around the holes and positive charges deposited at the rest of the area.

2.3 Electric attractive force measurement

The droplet is subjected to the electric attractive force (F_e) and drag force (F_d) during actuation. The drag force (F_d) is measured as shown in **Figure S14**a. The critical tilt

angle (θ_{c_1}) is obtained by changing the tilt angle of the paper until the droplet slides. According to **Equation S9**, the drag force ($F_{d_{(i)}}$) can be calculated.

$$F_{d_{(i)}} = \rho V_{(i)} g \sin\theta_{c_1} \tag{9}$$

where ρ is the density of the droplet, V is the volume of the droplet, and g is the acceleration of gravity.

The electric attractive force (F_e) is measured as shown in Figure S14b, and it is related to the applied voltage (U), the volume of the droplet (V), and the horizontal distance from the needle electrode (D). The critical tilt angle (θ_{c_2}) is obtained by changing the tilt angle of the porous paper until the droplet reaches a critical actuation state. According to **Equation S10**, the electric attractive force ($F_{e_{(i)}}$) can be calculated.

$$F_{e_{(i)}} = \rho V_{(i)} g \sin\theta_{c_2} + F_{d_{(i)}} \tag{10}$$

The measurement results of the electric attractive force are shown in **Figure S15**. It shows that increasing both droplet volume and applied voltage increases the electric attractive force and extends its range of action.

3. Droplet manipulation by charge graphics

3.1 Digital droplet manipulation by droplet pick-and-place robot

Digital droplet manipulation by droplet pick-and-place robot can be divided into three processes: volume-tunable droplet generation, pick, and place, as shown in **Figure S16**.

Volume-tunable droplet generation process. The droplets can not drop smoothly from the syringe needle because of the capillary force (F_c).

$$F_c = 2\pi R^2 \gamma_{LG} \cos\theta \tag{11}$$

where R is the radius of the syringe, γ_{LG} is the surface tension, θ is the contact angle. According to **Equation S11**, the capillary force (F_c) is constant and is related to the contact angle (θ) and the syringe radius (R). When the electric attractive force (F_e) is greater than the capillary force (F_c), the droplet can drop smoothly.

$$F_e = k\frac{q_1 q_2}{D^2} \tag{12}$$

where k is the electric attractive force constant, q_1 and q_2 are the quantity of the

droplet charges and the negative charges on the paper, D is their distance. Moreover, the charge amount of a droplet is approximately positively related to its volume. This means that the large volume has a large q_2, and a closer distance (D) can lead to smaller volume droplets. Thus, by tuning the horizontal distance (D) between the bottom needle electrode and the syringe needle, varied-volume droplets (V) are generated.

Droplet pick and place process. Droplet pick and place are realized by moving the bottom needle electrode and by turning off the power or increasing the value of H_2, respectively. The bottom needle electrode is installed on the gripper of the three-axis digital moving platform, the motion of which is programmable and controlled, and is known as the droplet pick-and-place robot.

3.2 Droplet splitting by boosting electric attractive force

The droplet splitting needs more large symmetric pulling forces than the droplet propelling. Herein, we realized droplet splitting by strengthening electric fields and reducing the gap between the bottom needle electrode and the papers, as shown in **Figure S17a**. We applied two separate bottom electrodes to form a negative charge bar under the droplet. By reducing the gap from 5 mm to 0.1 mm between the bottom needle electrode and the papers. Thus, the droplet is charged enough negatively to be deformed and split by significant pulling forces from opposite directions toward positive charge areas. A droplet with a volume of 10 μL is equally split, as shown in **Figure S17b**. By controlling the negative charge bar location, the splitting ratio can be modulated.

3.3 Reconfigurable droplet manipulation by configuring the bottom masks

3.3.1 Combining a mask with hole arrays and a moving baffle for droplet manipulation

A mask with hole arrays (diameter 2 mm) is pre-attached to the lower surface of the porous paper. A moving baffle is installed on the gripper of the three-axis digital moving platform and is placed close to the lower surface of the mask. The baffle is moved right to cover the left and middle columns of holes in turn, and the droplets deposited in the left hole are synchronously propelled from the left hole to the middle

and right hole, respectively.

3.3.2 Moving and rotating modular masks for droplet manipulation

Three modular masks (18 mm*6 mm) with hole arrays (diameter 1.5 mm) are attached to the lower surface of the porous paper and installed on the gripper of the three-axis digital moving platform, respectively. By programming the gripper to move or rotate the module mask, the droplet array distribution moves with it.

3.4 Droplet transport manipulation by designing the EPW channels

3.4.1 Sequential transport of droplets along straight-line and "S"-shape channels

The porous paper with the channel masks attached is placed vertically. The channel masks can be programmed by the gripper to switch from a straight-line channel to an "S"-shape channel. Sequentially injected droplets are trapped in the channel by the electric attractive force and accelerated by gravity to slide along the channel. In addition, by programmatically moving the gripper to decrease the value of H_2, droplets can be pinned above the bottom needle electrode due to the electric attractive force greater than gravity. **Figure S18a** shows that droplets being transported along the straight-line channel are pinned and mixed with subsequently transported droplets.

3.4.2 Guided transport of droplets in "Y"-shape channels

Changing the position of the bottom needle electrode can guide droplet transport. When the bottom needle electrode is moved to the main track of the "Y"-shape channel, the main track of the "Y"-shaped channel is defined as the output port, and the two bifurcated tracks are defined as the input ports. Droplets are injected from the input ports and transported along the two bifurcated tracks to the main track for mixing and output from the output port.

When the bottom needle electrode is moved to a bifurcated track in the "Y"-shape channel, the selected bifurcated track is defined as the output port, and the main track is defined as the input port. Droplets are injected from the input ports and transported along the main track and into the selected bifurcation track and output from the output

port.

In addition, when the bottom needle electrode is moved to the intersection of the "Y"-shape channel, the main track is defined as the input port. Sequential droplets are injected from the input port and transported along the main track until they are pinned in the middle of the channel intersection and mixed with subsequently transported droplets, as shown in **Figure S18b**.

3.4.3 Transport of multiple droplets in horizontal "D"-shape channels

Multiple droplets transport and mixing can be realized on horizontally placed porous paper with a mask of a "D"-shape channel. Similarly, the bottom needle electrode is moved to the intersection of the "D"-shape channel. The two droplets move along the straight-line and curved channels to the intersection of the channels for mixing, respectively, as shown in **Figure S19**.

3.5 Reconfigurable fluidic network for droplet color-matching

Figure 6d illustrates a reconfigurable fluidic network platform for droplet color-matching. The platform can be divided into three parts: the input side, the display side, and the control side. The input side consisting of micro syringe pumps is used to generate the primary droplets of four different colors (red, yellow, blue, and white). The display side consists of porous paper for real-time monitoring of the droplets. The control side consists of a mask film, a moving baffle, a micromotor, and a battery to control the order of color-matching and mask switching. The mask film including three kinds of patterns (M_1, M_2, and M_3) is installed on a pair of rotating shafts located below the porous insulating paper. The moving baffle is installed on the gripper of the platform located below the masks. The start-stop of the rotating shaft and the extension-retraction of the baffle are controlled by micromotors. The mask can construct EPW channels, and moving the baffle can dynamically change the constructed EPW channels. Thus, the combination of mask and baffle can switch droplet states (from pinned to sliding) for orderly color-matching and real-time decision-making of droplets.

When the mask film is switched to M_1, four droplets are input from the input side in turn. The red and white droplets move along the outer channels and are pinned at the intersection of two channels and mixed as light red. The yellow and blue droplets move along the middle channels and are pinned and mixed at the intersection to become green.

When the rotating shafts are rotated to switch the masking from M_1 to M_2, the red and yellow droplets move along the left channels respectively, and are pinned at the intersection to become orange. The blue and white droplets move along the right channels and are pinned at the intersection to become light blue. The controlling micromotor moves the baffle to move below the orange and light blue droplets. The two droplets are activated from the pinned state, slide down the new channels respectively, and mix as brown.

When the mask is switched from M_2 to M_3, red and yellow droplets move along the left channels respectively and are pinned at the intersection and mixed as orange. The orange color is activated to move to the second intersection and is pinned when the baffle is moved to the bottom of the orange droplet. The blue droplet is generated and slid along the channel until it mixes with orange droplets to become brown. The baffle is moved under the brown droplet. The droplet is activated to move to the third intersection and is pinned. The white droplet is generated and slid along the right channel until it mixes with the brown droplet to become light brown.

Figures

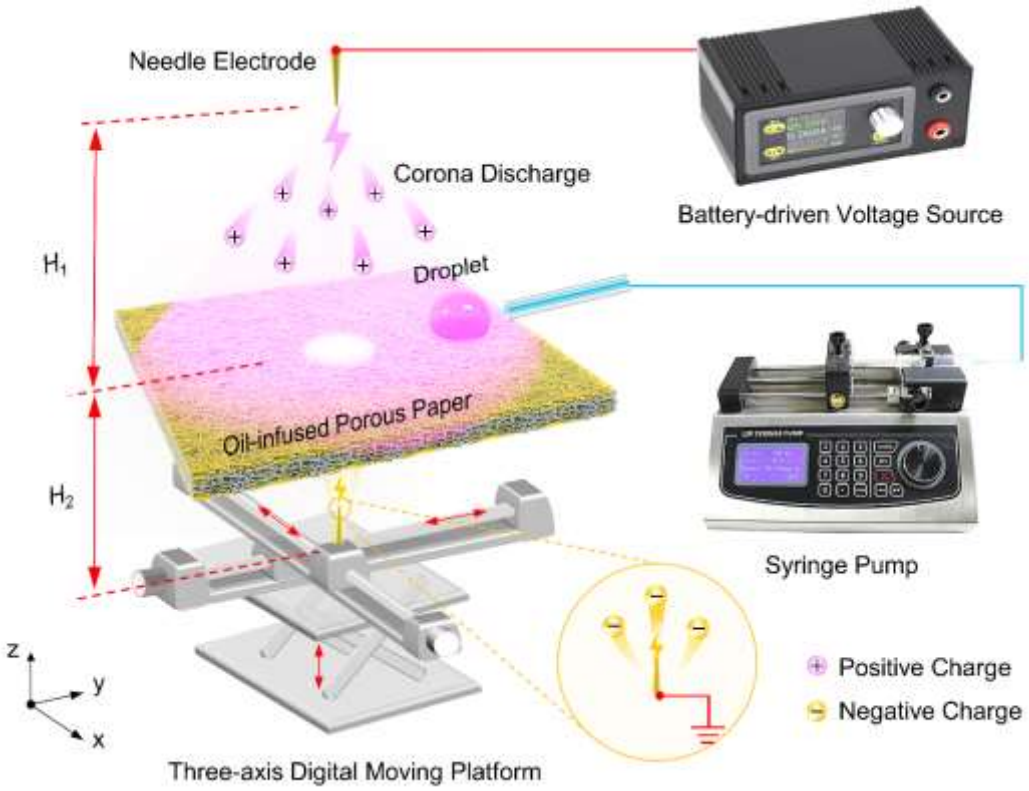

Figure S1. Schematic for the configuration of the droplet actuation platform.

Figure S2. Pictures of a battery-driven voltage source, consisting of a metal enclosure i), a high-voltage power module ii), and a lithium-ion battery iii).

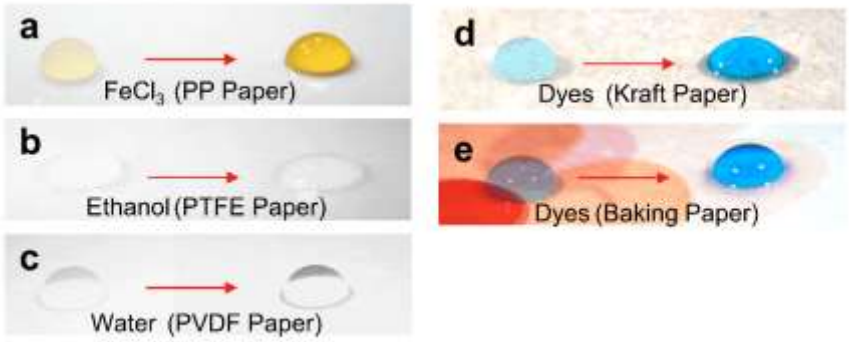

Figure S3. The universality of the droplet actuation platform in the aspect of droplet and paper selection. The time-lapse trajectory of a) $FeCl_3$ solution on PP paper, b) DI water on PVDF paper, c) alcohol on PTFE paper, and d-e) dyed water on kraft paper and baking paper.

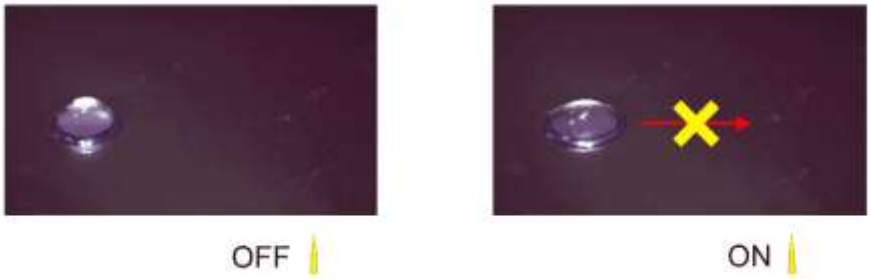

Figure S4. Optical pictures demonstrate that PET film without porous structures cannot actuate the droplet.

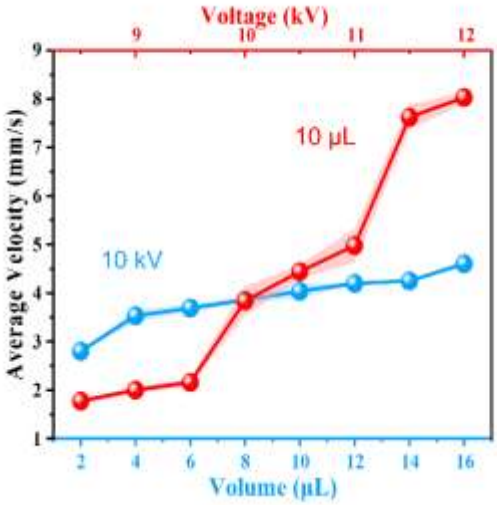

Figure S5. The effect of volume and applied voltage on the average velocity of droplet motion. It shows that the effect of applied voltage is more significant compared to droplet volume. Being different from the voltage-driven droplet manipulation methods, the present work is based on the surface charge density. The reason for the jump in the velocity-voltage correlation is the noncontinuous and nonlinear charge emission from the needle electrode as shown in Figure S7.

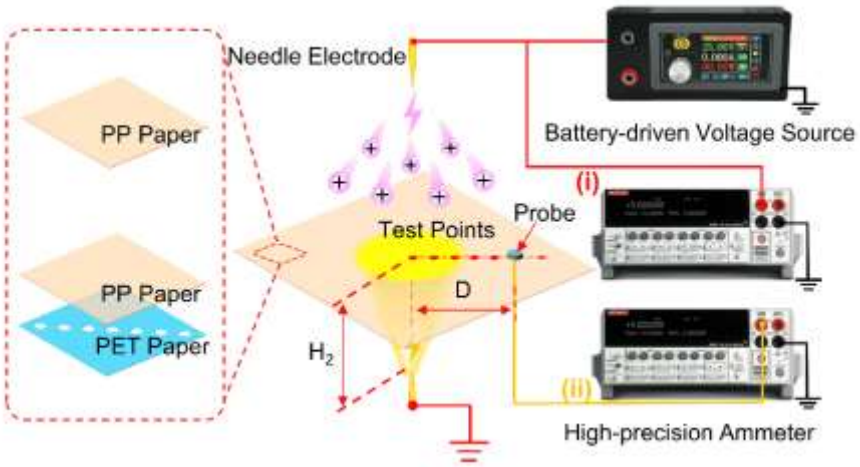

Figure S6. Schematic of online testing of the current of the needle electrode i) and the current on the PP paper surface ii).

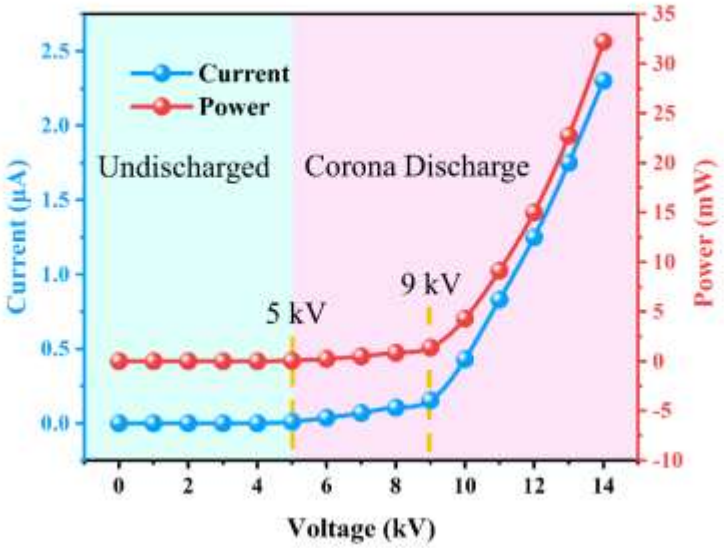

Figure S7. Relationship between the current of the needle electrode, power, and applied voltage. The distances of the top and bottom needles from the PP paper are 60 mm and 5 mm, respectively.

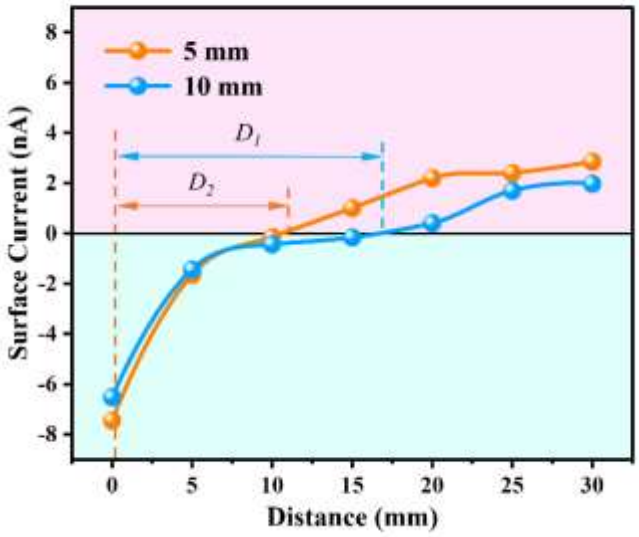

Figure S8. Surface current distributions at different locations on the PP paper. The distances of the bottom needles from the PP papers are 5 mm and 10 mm, respectively.

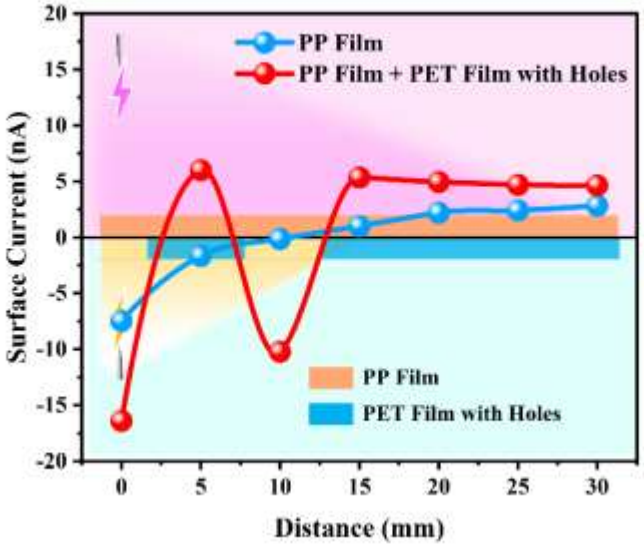

Figure S9. Comparison of surface currents of the PP paper with/without PET mask of inserting the hole array. The distances of the top and bottom needle electrodes from the PP paper are 60 mm and 5 mm, respectively. The diameters of the holes are 5 mm. The hole distance is 10 mm.

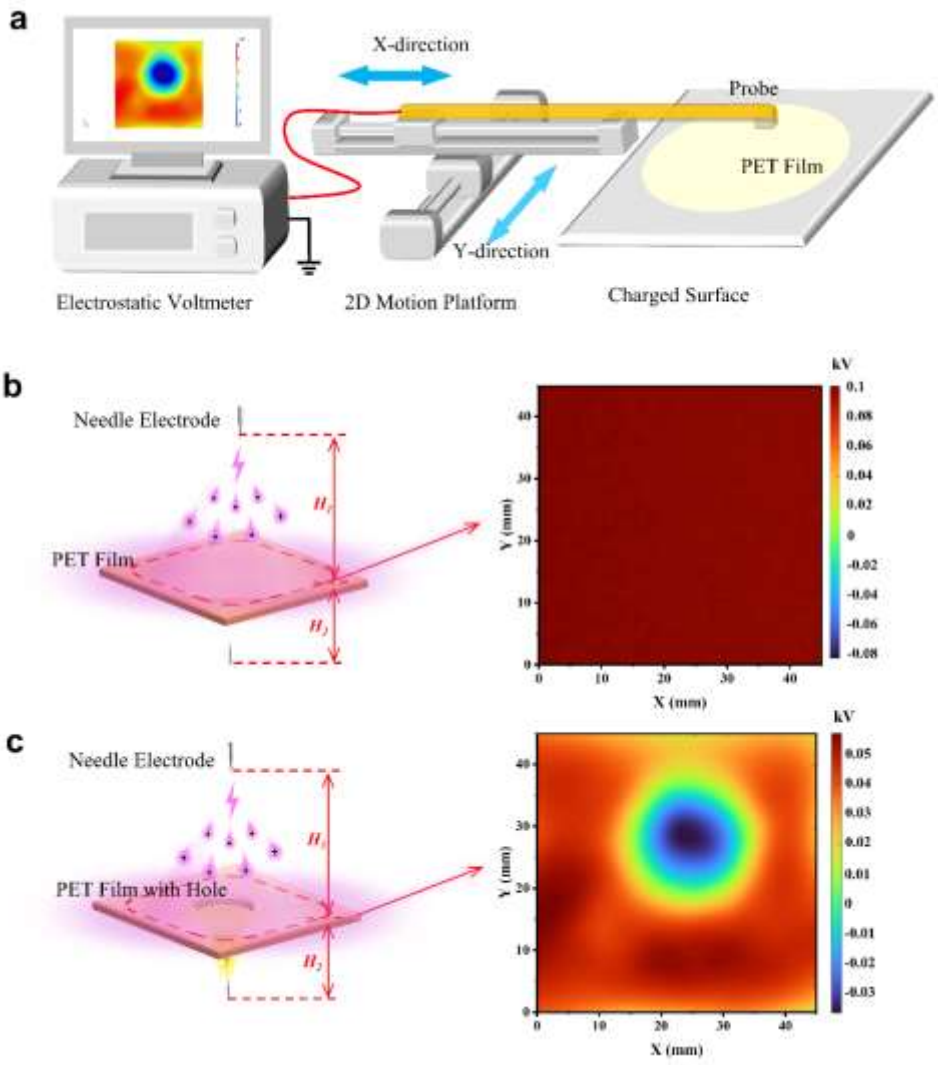

Figure S10. Surface potential measurement. a) Schematic of the scanning surface potential device. b) Surface potential distributions on PET film. The applied voltage is 9 kV. The PET film is charged for 2 minutes. c) Surface potential distributions on PET film with a hole. The PET film is charged for 2 minutes. The hole in the middle of the PET film is 3 mm in diameter. The distances between the top and bottom electrodes and the PET film are H_1 and H_2, H_1 = 60 mm and H_2 =5 mm, respectively. The applied voltage of the top needle is 9 kV, while the bottom needle is grounded.

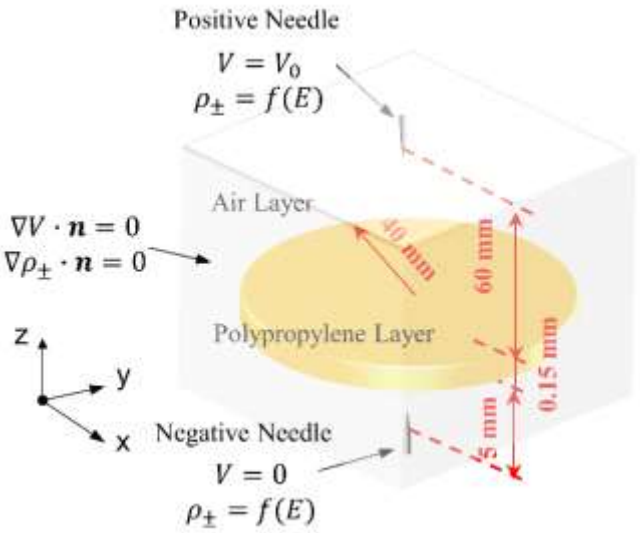

Figure S11. Simulation model of the considered domains and boundary conditions of the needled-needle electrodes doped with different dielectric layers.

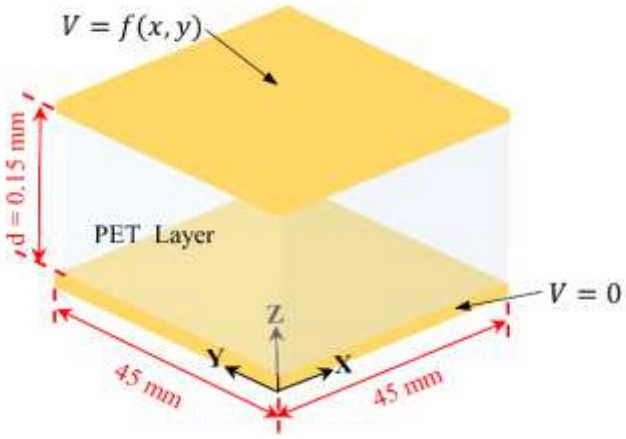

Figure S12. Simulation model for inversing the surface charge density of the PET film based on measured surface potentials in Figure S10b and c.

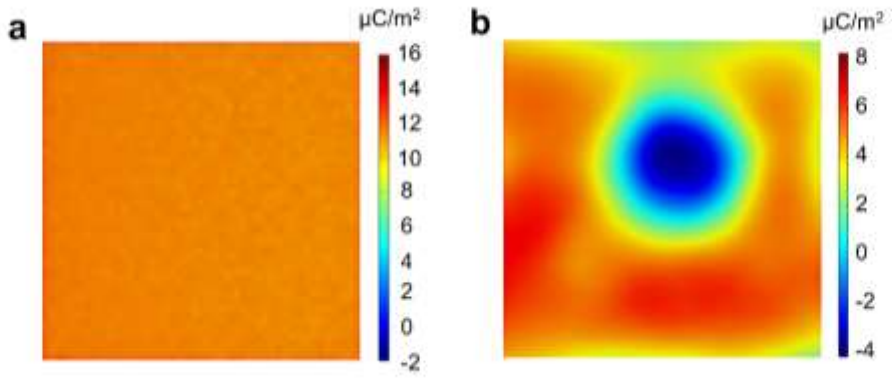

Figure S13. Simulated surface charge distributions based on measured surface potentials in Fig. S10b and c. a) Surface charge distribution of the PET film without the hole. b) Surface charge distribution of the PET film with a hole.

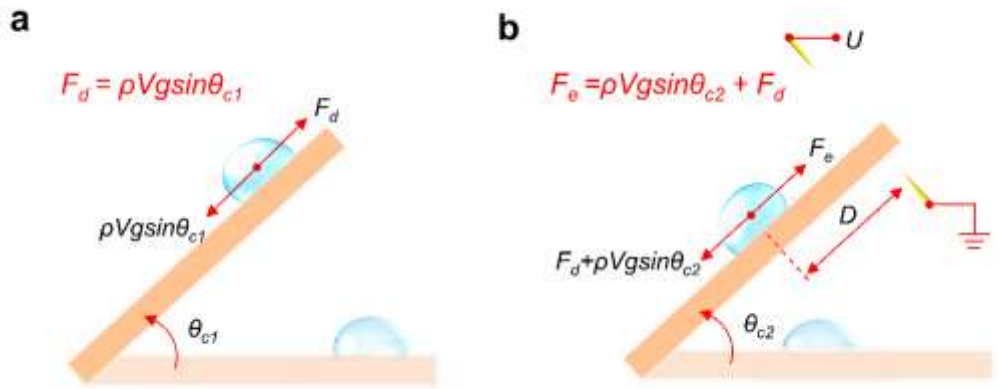

Figure S14. Schematic of force measuring methods. a) Drag force, F_d. b) Electric attractive force, F_e.

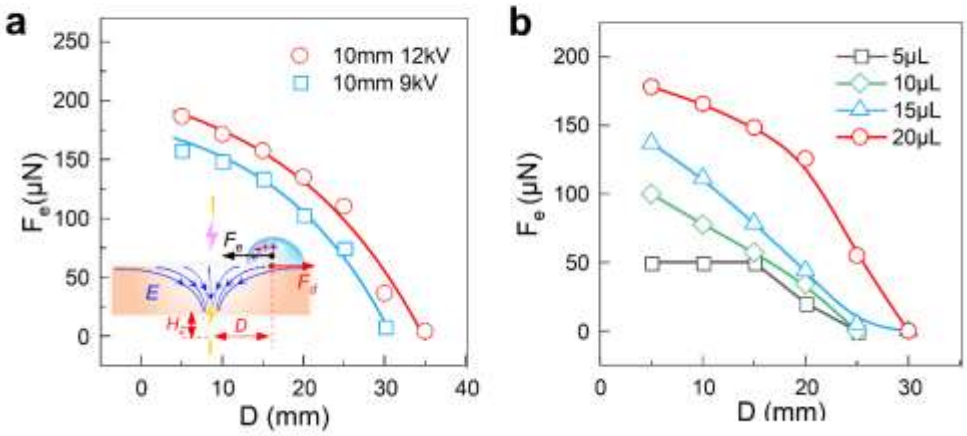

Figure S15. The effect of a) applied voltage and b) droplet volume on the measured electric attractive force exerted on the droplet.

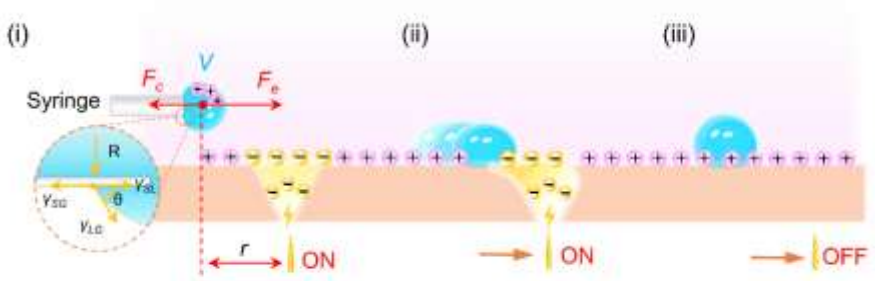

Figure S16. Schematic of volume-tunable droplet generation i), pick ii), and place iii) mechanism in digital droplet manipulation by droplet pick-and-place robot.

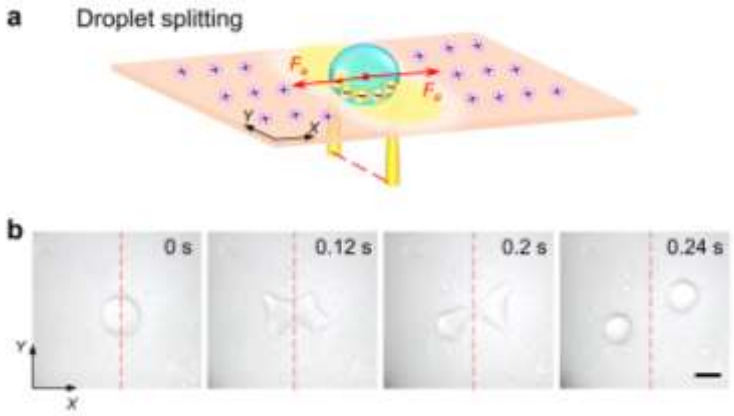

Figure S17. Schematic of the mechanism of droplet splitting in digital droplet manipulation a) and the splitting process b). Scale bars are 2 mm.

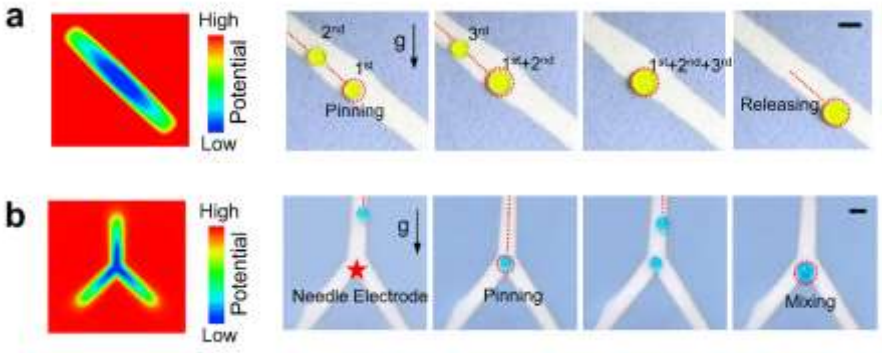

Figure S18. Droplet trapping at the middle of channels with saddle-shape EPWs. a) Straight-line channel. b) "Y"-shape channel. Scale bars are 2 mm.

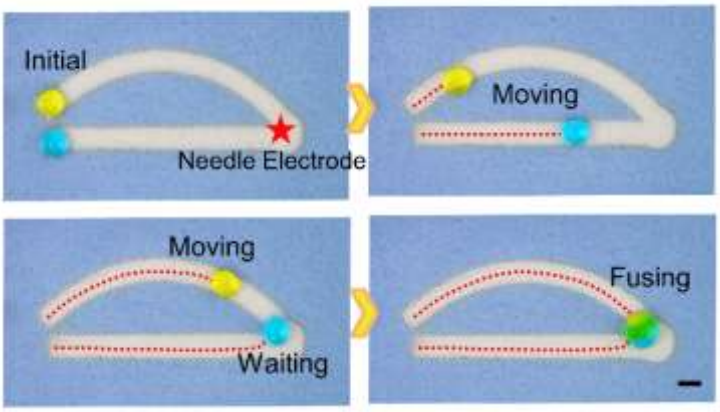

Figure S19. Droplet dynamics in “D”-shape channel with surface potential gradients on the horizontal porous paper. The scale bar is 2 mm.

Table S1. Comparison of this work with other studies[11,12] in droplet manipulation by our team.

	Work 1	Work 2	**This work**
Principle	Electrostatic levitation	Sliding barrier induced by nonconductive/conductive patterns	Surface charge graphics
Precise control	×	×	√
3D manipulation	√	×	√
Multiple droplets	×	√	√
High-throughput transmission	×	√	√
Unmodified surface	×	×	√
Unlimited distance	×	√	√
No carrier	×	√	√
Velocity	37 mm/s	\	83 mm/s
Volume range	10	10	10^5
Substrate tilt angle	0°	15°~90°	0°~90°

Movies S1 to S10

Supplementary Movie S1. Droplet actuation with opposite charge deposition.

Supplementary Movie S2. Digital droplet manipulation by dynamically writing charge graphics.

Supplementary Movie S3. Handling of multi-droplet enabled by droplet pick-and-place robot.

Supplementary Movie S4. Controllable and parallel trapping of the droplet array by projecting charge graphics.

Supplementary Movie S5. Sequential and high-throughput droplet transport in EPW channels.

Supplementary Movie S6. Reconfigurable droplet manipulation by configuring the bottom masks.

Supplementary Movie S7. Digitally controlled micro-reaction.

Supplementary Movie S8. Versatile droplet-actuated cargo transport.

Supplementary Movie S9. Large-size, rapid, and size-adjustable microdroplet collection and chemical detection.

Supplementary Movie S10. Reconfigurable fluidic networks for droplet color-matching.

References

[1] http://kvenjoy.com/#home.

[2] B. Du, Z. Hou, H. Xu, J. Li, and Z. Li, *High Voltage Engineering*. **2017**, *43*, 2769-2780.

[3] K. Adamiak, P. Atten, *J. Electrostat*. **2004**, *61*, 85.

[4] Y. Zhong, R. Kou, M. Wang, Y. Qiao, *J. Phys. D-Appl. Phys*. **2019**, *52*, 445303.

[5] https://www.comsol.com/multiphysics/electrostatics-theory.

[6] S. Chen, Y. Zhu, J. Tu, F. Wang, *J. Phys. D-Appl. Phys*. **2019**, *52*, 3652032.

[7] V. T. Dau, T. X. Dinh, C. Tran, T. T. Terebessy, T. C. Duc, T. T. Bui, *J. Aerosol Sci.* **2018**, *124*, 83-94.

[8] S. Z. Ahmed Dabbak, H. A. Illias, B. C. Ang, N. A. Abdul Latiff, M. Z. H. Makmud, *Energies* **2018**, *11*, 1448.

[9] F. W. Peek, *Dielectric Phenomena in High Voltage Engineering*, New York: McGraw-Hill, **1929**.

[10] N. A. Kaptsov, *Elektricheskie Yavleniya v Gazakh i Vakuume*, Moscow, OGIZ, **1947**.

[11] C. Liu, X. Liu, Q. Tang, W. Zhou, Y. Ma, Z. Gong, J. Chen, H. Zheng, S. W. Joo, *Anal. Chem.* **2022**, *94*, 8217-25.

[12] D. Fang, W. Zhou, Y. Jin, X. Liu, Y. Zeng, Z. Wang, H. Zheng, *Droplet*. **2023**, *2,* e74.